

Prismatic Confinement Induces Tunable Orientation in Plasmonic Supercrystals

Wajdi Chaâbani,[‡] Jieli Lyu,[‡] Jules Marcone, Claire Goldmann, Eleonora J. M. ten Veen, Clément Dumesnil, Thomas Bizien, Frank Smalenburg,* Marianne Impéror-Clerc,* Doru Constantin,* and Cyrille Hamon*



Cite This: *ACS Nano* 2024, 18, 9566–9575



Read Online

ACCESS |

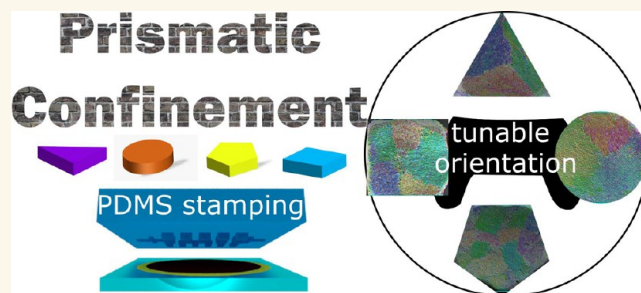
Metrics & More

Article Recommendations

Supporting Information

ABSTRACT: Throughout history scientists have looked to Nature for inspiration and attempted to replicate intricate complex structures formed by self-assembly. In the context of synthetic supercrystals, achieving such complexity remains a challenge due to the highly symmetric nature of most nanoparticles (NPs). Previous works have shown intricate coupling between the self-assembly of NPs and confinement in templates, such as emulsion droplets (spherical confinement) or tubes (cylindrical confinement). This study focuses on the interplay between anisotropic NP shape and tunable “prismatic confinement” leading to the self-assembly of supercrystals in cavities featuring polygonal cross sections. A multiscale characterization strategy is employed to investigate the orientation and structure of the supercrystals locally and at the ensemble level. Our findings highlight the role of the mold interface in guiding the growth of distinct crystal domains: each side of the mold directs the formation of a monodomain that extends until it encounters another, leading to the creation of grain boundaries. Computer simulations in smaller prismatic cavities were conducted to predict the effect of an increased confinement. Comparison between prismatic and cylindrical confinements shows that flat interfaces are key to orienting the growth of supercrystals. This work shows a method of inducing orientation in plasmonic supercrystals and controlling their textural defects, thus offering insight into the design of functional metasurfaces and hierarchically structured devices.

KEYWORDS: supercrystal polymorphism, small angle X-ray scattering, directed self-assembly, gold nanoparticles, Monte Carlo simulations, self-assembly in confinement



Nature has long inspired scientists with its ability to synthesize complex inorganic nanostructures by consistently exploiting the self-assembly in the confinement of (often complex) building blocks. This level of complexity has not yet been reached synthetically with colloidal crystals because most nanoparticles (NPs) are highly symmetric objects and because their self-assembly is unconstrained. In order to overcome this limitation, the NPs' shape and environment should be tuned to guide and “frustrate” crystallization.^{1–3} Aspects of self-assembly in confinement^{4–8} and shape-directed assembly^{9–15} have been studied separately and while acting together.^{16–23} Intricate structures can be engineered by exploiting the geometrical incompatibility between local ordering and the topology of the confinement geometry, as shown for some NPs and microparticles.^{5,12} For instance, cellulose nanocrystals,¹⁹ nanoplatelets,²⁴ nanospheres,⁶ and nanocubes¹⁶ have been assembled into complex structures within emulsions droplets via so-called spherical confinement. Although the confinement could be tuned to

some extent by controlling the size of the colloids and the volume fraction in the droplets, Laplace pressure does not allow for changing the confinement geometry. In a similar vein, NPs have been ordered in cylindrical confinement, but the nature of the templates restricted assembly on a curved interface.^{25–27} Recent studies have pointed out that the topology of orientational defects could be directed with flat interfaces and shown experimentally with microparticles such as silica rods²⁸ and viruses.²⁹ However, the potential of “prismatic confinement” to assemble anisotropic NPs has not yet been explored.

Received: December 19, 2023

Revised: February 27, 2024

Accepted: March 18, 2024

Published: March 20, 2024



Noble metal nanoparticles exhibit intriguing optical properties attributed to localized surface plasmon resonances, with frequencies highly dependent on nanoparticle composition, morphology, and the surrounding medium.^{30,31} The organization of gold NPs into ensembles leads to the emergence of new plasmon resonances unattainable by the individual particles, and the resulting optical properties can be further tuned and even enhanced.^{32–34} Hybrid top-down/bottom-up strategies can be used for integrating colloids into hierarchically structured devices effectively and at low cost.^{35,36} Those approaches include a collection of techniques based on contact printing and replica molding with an elastomeric stamp, whose structural features direct the deposition of the colloids onto the template or on a substrate of interest.^{5,37,38} Since their initial development, a broad range of colloidal materials have been formed by combining evaporation-induced self-assembly (EISA) and templating.^{4,39–43} Frequently, the template features consist of simple geometries (e.g., cylindrical cavities) and are in the same size range as the building blocks, resulting in the deposition of single NPs or in the formation of small clusters.^{44–47} Some recent developments include the formation and study of patterned plasmonic superlattices for lattice plasmon resonance^{48–53} and sensing applications.^{46,54–59} Some work reported the self-assembly of supercrystals within large cavities,^{55,60–62} but local ordering and the detailed orientation of NPs in the assembly were not explored, presumably because of the challenges in probing the order at different length scales in the material. Overall, controlling the ordering of anisotropic nanoparticles in confinement by template-assisted assembly holds significance from fundamental interest in the development of future plasmonic metasurfaces. In this context, understanding the impact of the template geometry on the final structure of the supercrystals would be an important advancement.

In this study we explore how the shape of nanoparticles and a tunable confinement influence the self-assembly of supercrystals. The assembly of the supercrystals is directed by a microtextured template featuring an array of prismatic cavities with varying polygonal cross-section. Conventional small-angle X-ray scattering (SAXS) and microbeam SAXS (μ SAXS) are employed for large-scale orientation analysis, while scanning electron microscopy (SEM) provides real-space local structural characterization. Our findings reveal that the mold interfaces direct the growth of multiple crystal domains, demonstrating that the confinement geometry controls both the number and the orientation of the monodomains.

RESULTS AND DISCUSSION

Gold nanorods (AuNRs) were obtained by seed-mediated growth and were uniform in size and shape (length 55 ± 5 nm, width 18 ± 2 nm, Figure S1). Self-assembly was conducted by confining a drop of the AuNR suspension between a substrate (silicon wafer or glass slide) and a polydimethylsiloxane (PDMS) template and letting it dry under ambient conditions (Figure 1A). The PDMS templates comprised an array of prismatic cavities with a fixed depth of $2 \mu\text{m}$ and various cross sections (circle, triangle, square, pentagon and hexagon) denoted hereafter by their rotational symmetry, i.e., C_∞ , C_3 , C_4 , C_5 , and C_6 , respectively (Figure 1B). For supercrystals, we use the same symmetry notation, followed by the SC suffix. After confinement and evaporation induced self-assembly, the template is peeled off to leave on the substrate well-ordered superlattices of prismatic SCs (Figure 1C).

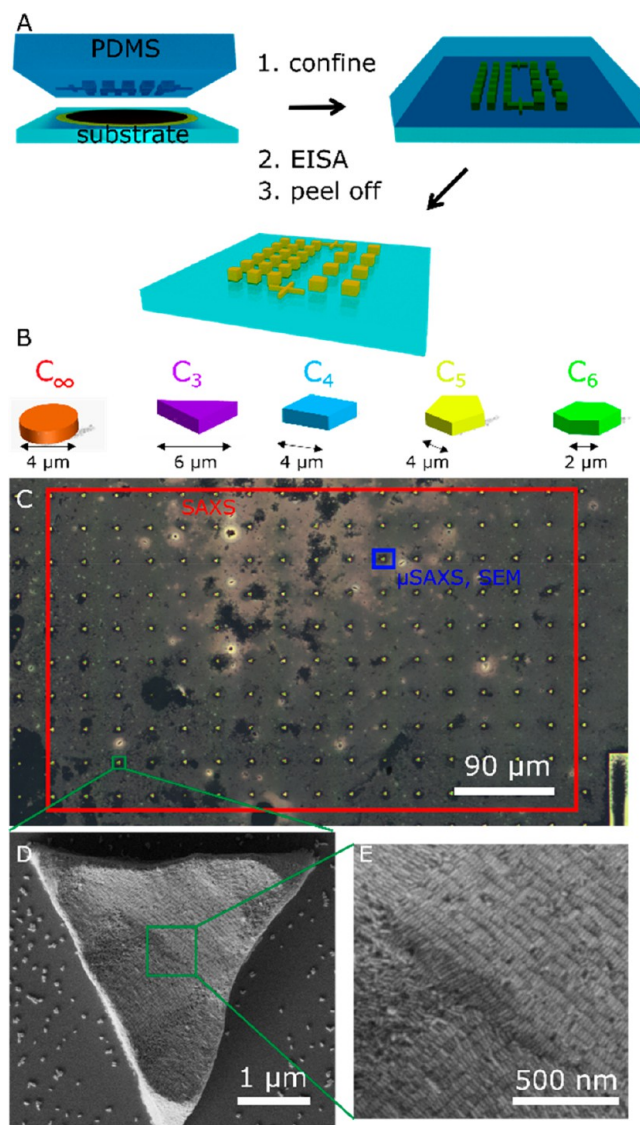


Figure 1. Principle of the method. (A) Schematic view of the templated EISA process. (B) Schematic description of the shape and size of microcavities, whose cross sections are denoted by their rotational in-plane symmetry. (C) Optical microscopy image of a superlattice of triangular SCs obtained after template-assisted self-assembly and peeling off the PDMS template. The red frame shows the typical footprint of the conventional SAXS beam, and the blue one that of the μ SAXS beam, which also corresponds to the size of an SEM image. (D, E) SEM images of a AuNR triangular SC viewed at different magnifications.

We used a multiscale characterization strategy, as illustrated in Figure 1C. Full-beam SAXS was used to characterize the structuration over large length scales, by averaging over hundreds of supercrystals. SEM image analysis revealed the organization of the NPs at the supercrystal surface. Combining high spatial resolution to study individual supercrystals as well as screening the structure of many supercrystals for statistical significance is a technical challenge that cannot be solved either by SEM or by full-beam SAXS.⁶³ In order to achieve this result, a synchrotron microbeam SAXS (μ SAXS) technique is implemented to study the structuration of many individual supercrystals. In the following, we investigated the structure of the AuNR supercrystals by this multiscale approach, beginning with SEM characterization (Figure 2).

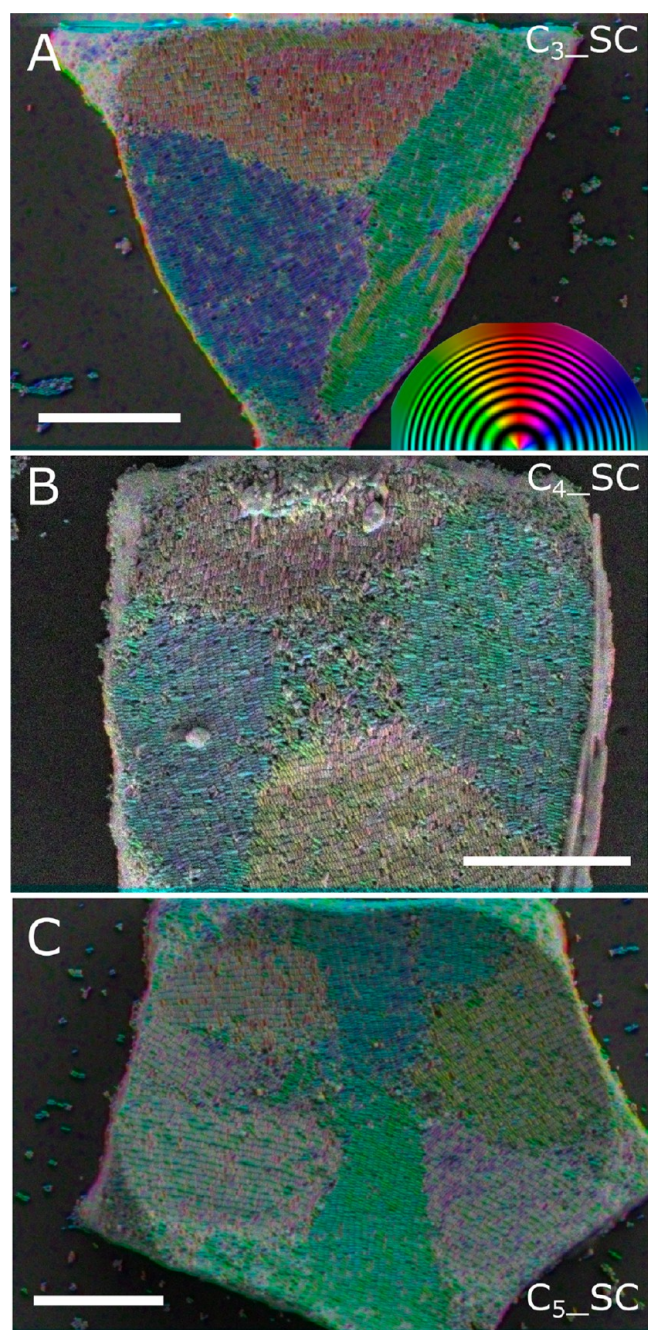


Figure 2. Prismatic supercrystals with templated monodomain orientation. (A–C) SEM images of prismatic SCs with C_3 , C_4 , and C_5 symmetry, respectively, composed of self-assembled AuNRs. AuNRs are color-encoded according to their orientation for ease of identification of the monodomains. The nanorods' long axis is found to be either perpendicular (C_3 _SC, C_4 _SC) or parallel (C_5 _SC) to the prism facets. Scale bar is 1 μm for all images.

In all SEM images, the long axis of most nanorods was parallel to the substrate. SEM image analysis was performed to color-code AuNRs according to their orientation for C_3 _SC, C_4 _SC and C_5 _SC (Figure 2). The angular color code is the inset in Figure 2A. This set of experiments shows that prismatic cavities direct the formation of ordered and oriented monodomains of AuNRs. For instance, three monodomains with orientations evenly spaced by $2\pi/3$ can be observed for C_3 _SC. In contrast, four monodomains $\pi/2$ apart were

observed for C_4 _SC. Similarly, consecutive edges of the C_5 _SC generate monodomains related by $2\pi/5$ rotations. However, inspection of many SEM images revealed structural heterogeneities, consisting of varying number of domains and orientational defects (see Figures S2–S4). To better understand the templating effect of the prismatic cavities on the distribution of orientational defects at the ensemble level, we performed full beam SAXS (Figure 3).

On the average, all prismatic supercrystals were highly oriented as shown by discrete Bragg spots on the 2D-SAXS images (Figure 3A). In contrast, C_∞ _SC displayed a ring-shaped scattering pattern, indicating the absence of a preferential monodomain orientation by cylindrical confinement. Although each measurement consists on averaging the scattering signal of hundreds of SCs, the number of Bragg spots is correlated with the rotational symmetry of the supercrystal: C_3 _SC, C_4 _SC, C_5 _SC, and C_6 _SC exhibited 6, 4, 10, and 6 Bragg spots, respectively. Azimuthal integration revealed large differences in the crystallographic orientation across the different prismatic supercrystals (Figure 3C). Via autocorrelation analysis of the SAXS curves (Figure 3D), their periodicity was determined to be $\pi/3$, $\pi/4$, $\pi/5$ and $\pi/3$ for C_3 _SC, C_4 _SC, C_5 _SC, and C_6 _SC, respectively. In SAXS, each AuNR monodomain gives rise to two equal Bragg spots related by a π rotation, as per Friedel's law. Supercrystals with an odd number of edges, here noted k , such as triangles and pentagons, exhibited $2k$ regularly spaced Bragg spots, whereas the ones with an even number of edges, such as squares and hexagons, only displayed k Bragg spots, since in this case two monodomains share an orientation and thus a pair of Bragg peaks. These results imply that each edge of the prism directs the growth of one monodomain (frequently with the rods perpendicular to the interface),^{62,64} which then grows until encountering another monodomain and forming a grain boundary. In line with this, no adjacent domains shifted by $\pi/2$ were noted for C_3 _SC, suggesting that the growth starts only from the edges and not epitaxially from the grain boundaries. We conclude that the number of edges of the cavity controls the number and orientation of monodomains in SCs. We next investigated in more detail the structure of the supercrystals (Figure 4).

Combined SEM and μSAXS analysis was performed on a C_4 _SC comprising a single monodomain, for ease of analysis (Figure 4A). Fast Fourier transforms (FFT) of the SEM images correspond to a 2D image analysis, whereas μSAXS corresponds to a 3D structural characterization. The similarity in the number of spots and their distribution between the FFT and μSAXS images indicates that the ordering observed on the supercrystal surface is representative of the supercrystal structure in volume (Figure 4B,C). This was confirmed on tilted SEM images, where approximately 15 organized layers of AuNRs were observed (Figure S5). In 2D, a centered rectangular lattice is evidenced in both the real and reciprocal space. We initially assumed that the structure of the crystals was hexagonal compact or smectic B, which corresponds to interlayers stacking in a hollow site fashion or to interlayer stacking without registry between the layers, respectively, as reported in many works. Instead, we infer the lattice to be orthorhombic from the absence of the a^*+2c^* reflection on the 2D μSAXS image, in which the expected position is indicated as an open red circle in Figure 4C. In comparison with the hexagonal compact structure, the orthorhombic structure corresponds to the intercalation of the hexagonal layers in a

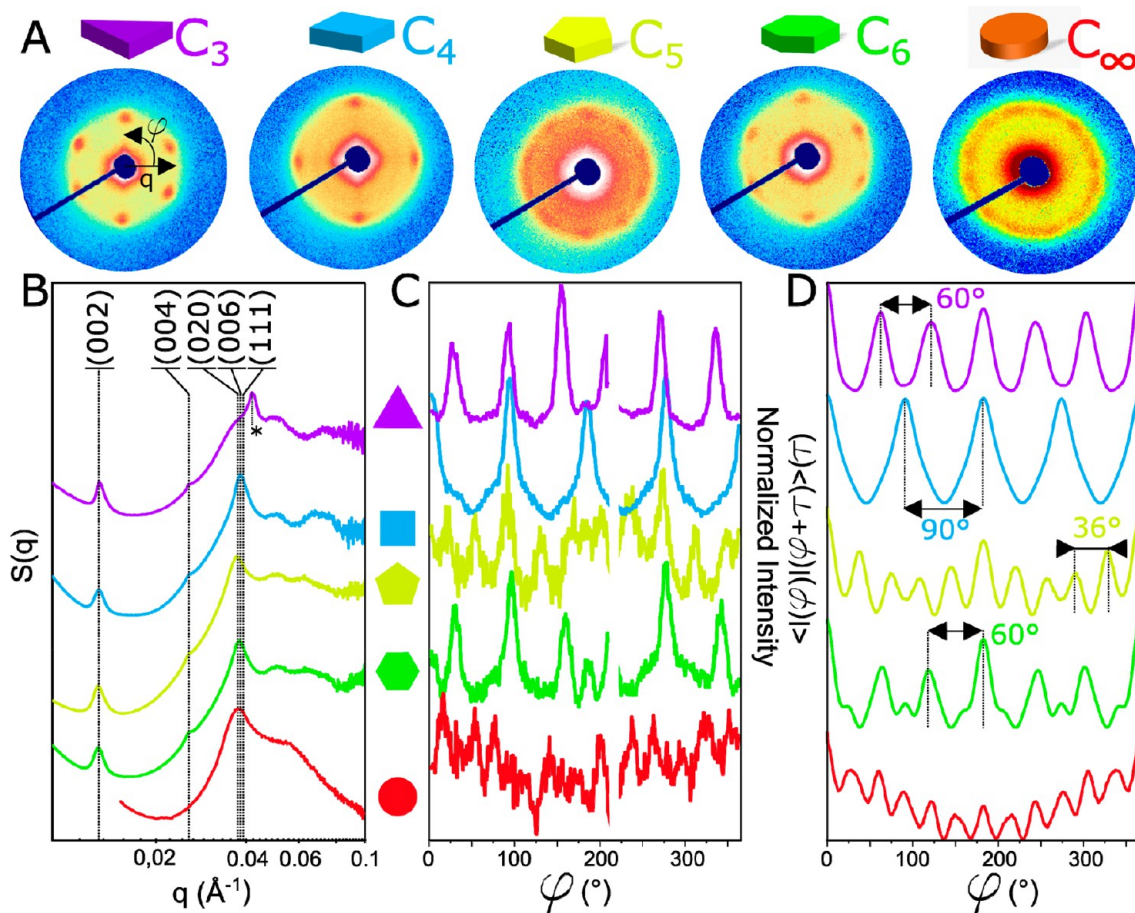


Figure 3. Average structural characterization over hundreds of AuNR supercrystals. (A) Two-dimensional SAXS images acquired on different zones of the sample consisting of AuNR supercrystals with different cross-section. The SAXS beam footprint is about $300 \times 300 \mu\text{m}^2$. SAXS images are shown on a logarithmic intensity scale. (B) Corresponding structure factors $S(q)$ of the supercrystals. Vertical lines indicate the expected positions of the Bragg peaks for an orthorhombic crystal. (C) Corresponding azimuthal integration $I(\varphi)$ at $q = 0.037 \text{ \AA}^{-1}$. (D) Autocorrelation analysis of $I(\varphi)$ to confirm the periodicity of the signals.

bridge site stacking fashion (Figure 4D). This last configuration is presumably preferred because all nanorods within the bottom layer are in contact with the substrate.

To bridge the gap between local and macroscale characterization, μSAXS was performed by scanning the SC lattice and acquiring one μSAXS image per SC. Azimuthal integration was performed on the 2D μSAXS images to retrieve the angular distribution of the Bragg peaks. We opted for a representation employing arrows, where relevant information, including the number and orientation of the domains as well as the extent of order, is encoded through color, direction, and length, respectively (Figures S6 and S7). The orientation is indicated in the angular range $[0, 2\pi/k]$ and the extent of order is determined from the intensity of the corresponding peak in the correlogram. Amorphous structures are marked by a white dot. The background optical image is acquired in situ during the μSAXS measurement. Four types of samples are compared using this representation in Figure 5: drop-cast SC (no template), C_{∞} _SC, C_3 _SC, and C_4 _SC.

In the drop-cast sample, the region within the coffee ring exhibited the highest degree of ordering, displaying a preferred orientation compared to the central region (Figures 5A and S8). However, the sample demonstrated heterogeneity, featuring small ordered domains of AuNRs, as indicated by the short length, random colors, and directions of the arrows.

This μSAXS result on drop-casted samples aligns with other SEM studies highlighting ordering at the edge of the deposits.^{10,65} For the C_{∞} _SC the distribution of SCs is more homogeneous across the array but the number of domains and their orientation vary from SC to SC (Figure 5B). Although an array of supercrystals is obtained in a cylindrical confinement, our results show that prismatic confinement allows better control over the number of domains and their orientation. For instance, the C_3 _SC consisted mainly in three symmetrically oriented domains, confirming the results obtained by full beam SAXS (Figure 5C). While the full beam analysis is only sensitive to ensemble ordering, the benefit of μSAXS is its ability to detect sample heterogeneities, defects, and amorphous regions (Figure S10). Some SCs with two or five oriented domains and a few amorphous SC were randomly scattered among the C_3 _SC. Similarly, the C_4 _SC are mainly characterized by two orientations across the array, with some occurrence of other nanostructuration (Figure 5D). Overall, the multiscale structural characterization of the samples by SEM, SAXS, and μSAXS shows that prismatic confinement can be used to control the formation and the orientation of plasmonic supercrystals arrays.

In the experiments, our ability to create smaller cavities is restricted by the resolution of photolithography, with minimum size features of around $2 \mu\text{m}$ in edge length, as

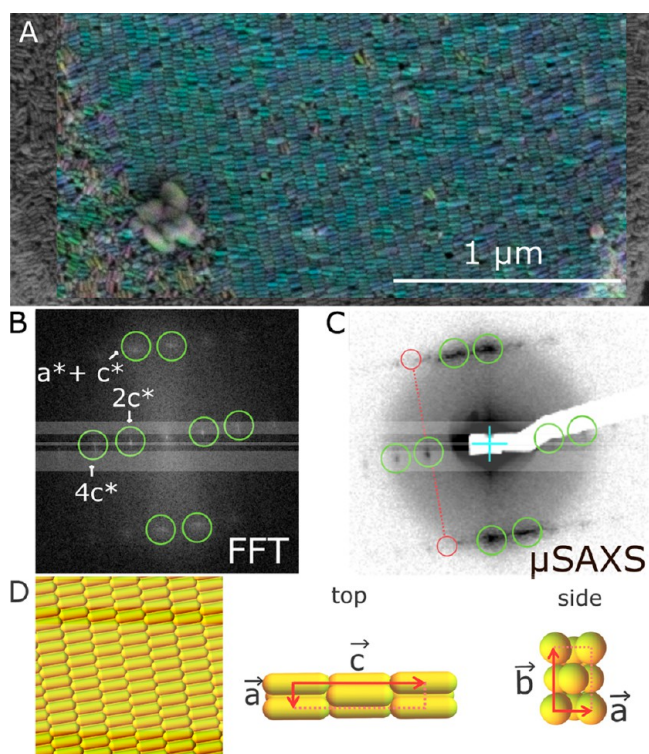


Figure 4. Small-scale characterization of a C_{4_SC} AuNR supercrystal. (A) SEM image of a supercrystal of AuNRs composed of a single monodomain. AuNRs are color-encoded with their orientation. (B) Corresponding fast-Fourier transform (FFT) of the SEM image. (C) μ SAXS image of the same supercrystal (shown on a logarithmic intensity scale). The red circles indicate the expected position of Bragg spots for a hexagonal lattice, which is missing here. The μ SAXS beam footprint is about $20 \times 20 \mu\text{m}^2$. (D) Schematic description of the AuNR orthorhombic lattice.

indicated by the manufacturer. To explore the effects of smaller cavities, we perform computer simulations of hard rods confined in prism-shaped cavities with either a triangular or square ground plane (from 550 to 825 nm in edge length). In the event-driven molecular dynamics simulations,^{66,67} the particles start off in a disordered configuration at low packing fraction and are then gradually compressed to high densities by slowly moving down the top confining plate. The systems consist of $N = 1000$ to 5000 spherocylinders with aspect ratio $L/D = 3.17$, where L is the tip-to-tip length and D is the rod diameter. Typical results are shown in Figure 6 for different system sizes. In contrast to the experiments, the rods in the triangular cavities clearly favor vertical alignment, i.e., perpendicular to the substrate rather than parallel. We attribute this to the fact that in these systems, formation of the smectic layering always starts in the corners of the triangle, where the two vertical walls meeting at an angle of 60° are highly compatible with the structure of a hexagonally ordered layer of vertically aligned rods. This bias is expected to be weaker in larger cavities, where most of the system is far away from the corners of the triangles (which are also less sharply defined), as observed experimentally. In the square cavities, this strong bias is not present, and we observe domains oriented along all three cardinal directions (i.e., along the edges of the box), typically resulting in multiple competing domains in the same simulation. Note that Figure 6 shows results at the packing fraction, where the particles are maximally ordered: further

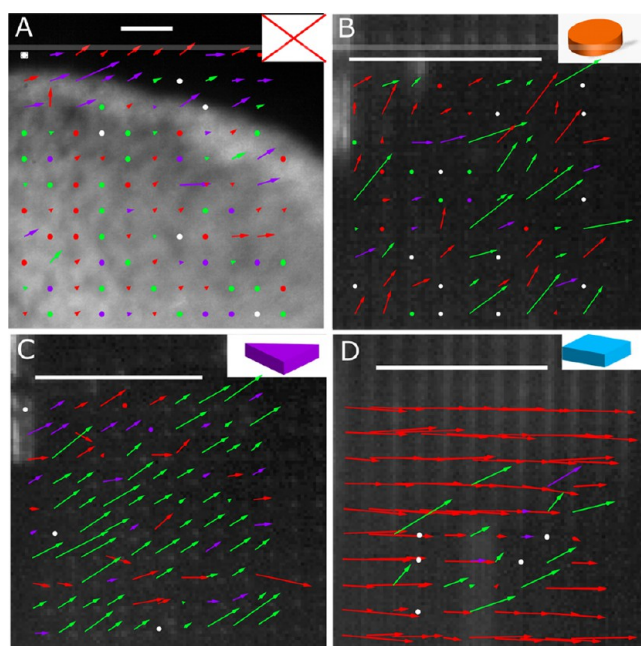


Figure 5. Structural characterization by μ SAXS of AuNR assemblies for varying template geometries. (A) No template (drop-casted), (B) C_{∞_SC} array, (C) C_{3_SC} array, and (D) C_{4_SC} array. The arrows encode the number and orientation of the domains, as well as the extent of order by their color, direction, and length, respectively. C_3 , C_4 , and C_5 domains are labeled as green, red, and purple, respectively. White points mark amorphous structures. The scale bar is $200 \mu\text{m}$ on all images.

compression typically leads to a tilt in the layers of vertically aligned rods, reducing the overall alignment with the walls (Figure S11). Our model explores shaping materials by nesting shapes and considers only steric interaction between the walls and the NPs. Although minimalistic, the model accurately reproduce the main experimental observations and thus captures the essential physics behind the phenomenon. Experimentally, PDMS is known to be hydrophobic with a water contact angle of $\approx 110^\circ$,³⁸ thus the NPs suspension was likely not to fully wet the cavities and form a meniscus during assembly. In agreement with this interpretation, the lateral dimension of the supercrystal was smaller than that of the cavity (e.g., $\approx 3 \mu\text{m}$ for the C_{4_SC} dried in cavities with a $4 \mu\text{m}$ square cross section). Other studies pointed out that the shape of the supercrystals can display rounded profiles,^{61,62} which may be seen as reminiscent of a meniscus formed at the triple contact line between air, the solution, and the substrate. While PDMS has an impact on the shape of the supercrystal, it does not directly affect the local ordering of the nanoparticles because assembly takes place preferentially at the air/water interface rather than at the PDMS/water interface.

We next performed the templated assembly of AuBPs (length $66 \pm 4 \text{ nm}$, width $25 \pm 2 \text{ nm}$, Figure S12 and Figure 7A). SEM image analysis reveals the formation of AuBPs supercrystals, characterized by multiple monodomains (Figures 7B–D, S13, and S14). 2D SAXS images were very similar to those obtained with AuNRs in terms of the number and distribution of Bragg spots, implying that the microcavity edges also template the growth of oriented AuBPs monodomains (Figure 7E). This experiment shows that supercrystals composed of other nanoparticle shapes can also be oriented within prismatic cavities.

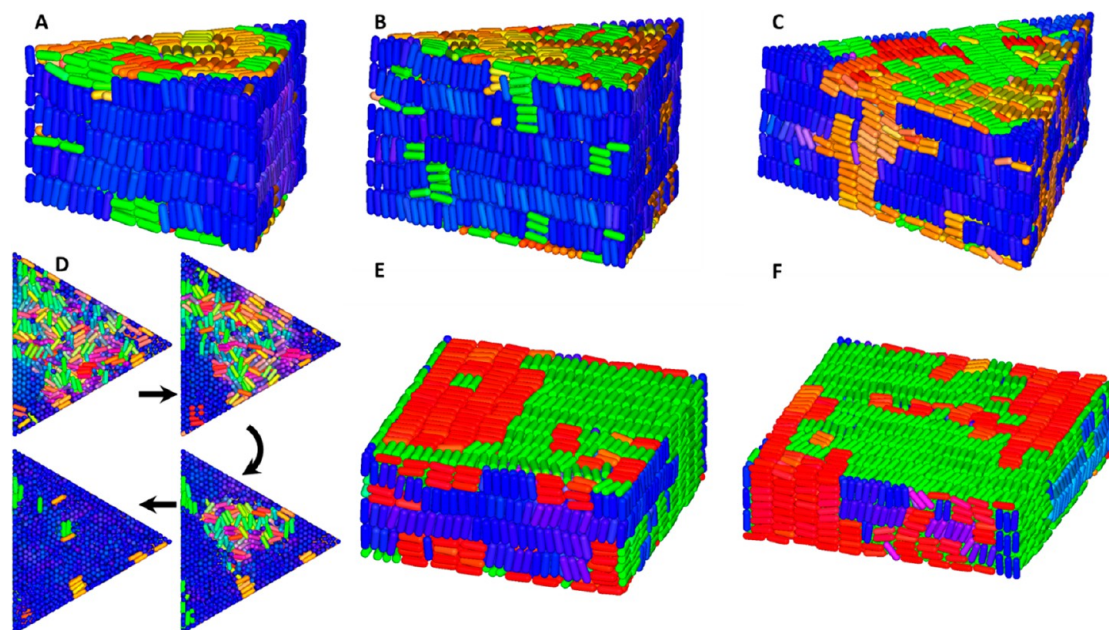


Figure 6. Self-assembly of confined hard spherocylinders in simulations. (A–C) Configurations after compression inside triangular geometries with varying edge lengths of the ground plane ($L_{\text{box}} = 10L, 12.5L, 15L$ for A, B, and C, respectively), and the number of particles chosen to obtain an approximately equally thick final result ($N = 2000, 4000$, and 5000 , respectively). (D) Time development of the internal ordering in a typical system ($L_{\text{box}} = 12.5L, N = 4000$), showing a horizontal cut through the box at different times, as indicated by the arrows. Note that crystallization starts from the corners. (E, F) Same as (A)–(C), but for confinement in a square prism: (E) $L_{\text{box}} = 10L, N = 4000$, (F) $L_{\text{box}} = 12.5L, N = 5000$.

CONCLUSIONS

Anisotropic gold nanoparticles were assembled within prismatic cavities by evaporation-induced self-assembly. Using a multiscale characterization methodology, we infer design rules for the formation of prismatic SC with a tailored orientation by changing the confinement geometry. Locally, SEM images show the anchoring of gold nanorods to the edges of the cavities, forming SCs with varying numbers of oriented monodomains and controlled texture. SAXS analysis confirmed the preferred orientation of the monodomains over hundreds of supercrystals. μ SAXS mappings revealed some structural heterogeneity but overall confirm that this approach provides oriented SCs in high yield. Numerical simulations of hard rods compressed inside a hard prism-shaped confinement show similar domain formation but display a stronger propensity to align vertically, especially inside triangle-shaped cavities. This difference is likely due to the relatively smaller cavity sizes, perfectly flat walls, and sharp corners used in the simulations. The results demonstrate the growth of multiple crystal domains influenced by the mold's interface, where each side directs the growth of a monodomain until it encounters another, resulting in grain boundary formation. Since our approach for orienting supercrystals works for AuNRs and AuBPs, we hypothesize that it can be generalized to NPs superlattices of other relevant shapes such as pentagonal nanoprisms,⁶⁸ platonic solids^{11,69} and nanoplatelets.⁷⁰ Although cylindrical microcavities do not allow controlling of the orientation of anisotropic colloids, this work shows that prismatic cavities are promising to orient such nanoparticles on a substrate. In plasmonics, engineering supercrystals with some preferred orientation could be useful for rendering a metasurface sensitive to light polarization, a direction we are currently exploring. Beyond plasmonics, orienting perov-

skites^{39,71} or other semiconducting nanocrystals^{72–74} within assemblies could lead to amplified and directional emission.

EXPERIMENTAL SECTION

Materials. All chemicals were obtained from Sigma-Aldrich and used without further purification: hexadecyltrimethylammonium bromide (CTAB, $\geq 99\%$), hexadecyltrimethylammonium chloride (CTAC, 25 wt % in H_2O , 90%), hydrogen tetrachloroaurate trihydrate ($\text{HAuCl}_4 \cdot 3\text{H}_2\text{O}$, $\geq 99.9\%$), silver nitrate (AgNO_3 , $\geq 99.0\%$), 5-bromosalicylic acid (S-BrSA, 90%), L-ascorbic acid (AA, $\geq 99\%$), sodium borohydride (NaBH_4 , 99%), and trisodium citrate dihydrate ($\geq 99.0\%$). Water purified by reverse osmosis with a resistivity ($>15 \text{ M}\Omega\text{-cm}$) was used in all experiments.

AuNR Synthesis. AuNRs were synthesized according to previously reported methods.⁷⁵ For the preparation of the seeds, 50 μL of 0.025 M HAuCl_4 solution was added to 4.7 mL of 0.1 M CTAB solution, and after mixing, 300 μL of freshly prepared 0.01 M NaBH_4 solution was injected under vigorous stirring. The color of the solution changed from yellow to brownish-yellow and then stirring was stopped after 2 min. The seed solution was aged at 30 $^\circ\text{C}$ for at least 30 min before injection into the growth solution. The growth solution was prepared by mixing 125 mL of 0.1 M of CTAB with 225 mg of S-BrSA, 2.38 mL of 0.01 M AgNO_3 , 120 mL of H_2O , and 5 mL of 25 mM HAuCl_4 solution. The process of prereduction was monitored by absorbance spectroscopy, and when the absorbance at 396 nm reached 0.65, 650 μL of 100 mM AA solution was injected quickly under fast stirring. When the solution turned colorless, 400 μL of previously synthesized seed solution was added quickly, and the mixture was then kept at 30 $^\circ\text{C}$ for 4 h. After synthesis, the suspension was purified by 2 rounds of centrifugation (6000 rpm, 40 min) to remove the excess CTAB and then redispersed in 2.5 mM CTAC solution.

AuBP Synthesis. AuBPs were synthesized by a seed-mediated growth method adapted from the literature.⁷⁶ For the synthesis of the pentatwinned seeds, 33 mL of a 60.6 mM CTAC solution was prepared in a 100 mL Erlenmeyer flask, in which 400 μL of 25 mM HAuCl_4 and 4 mL of 50 mM sodium citrate were added in sequence

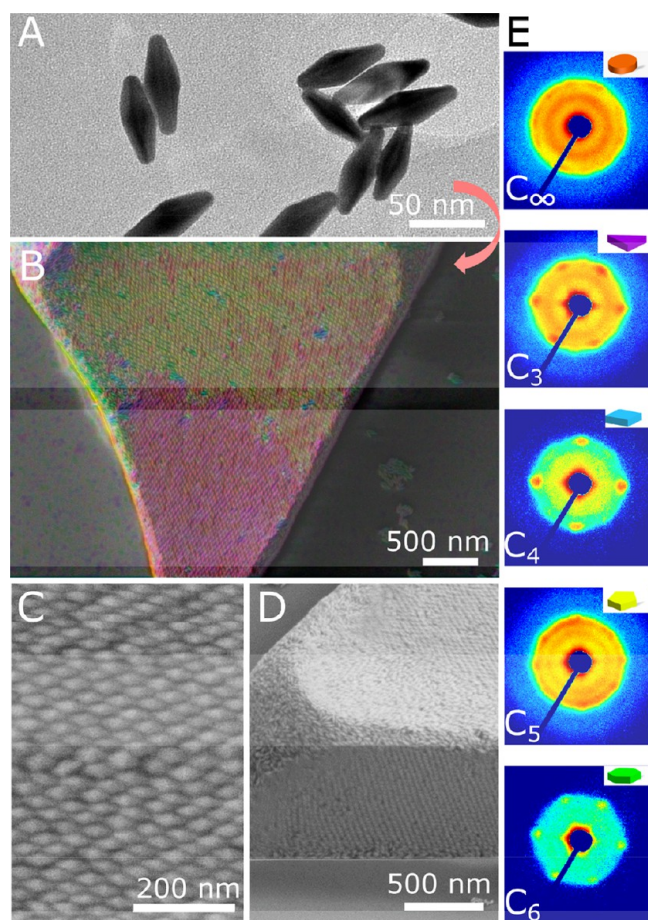


Figure 7. Multiscale characterization of AuBPs prismatic supercrystals. (A) Two-dimensional SAXS images acquired at different cross sections of the sample consisting of supercrystals with different cross sections. The SAXS beam footprint is about $300 \times 300 \mu\text{m}^2$. SAXS images are shown on a logarithmic intensity scale. (B) TEM image of AuBPs. (C–E) SEM images viewed at different magnifications and orientation. In (C), AuBPs are color encoded with their orientation for ease of identification of the monodomains.

under gentle stirring. The solution was kept in a water bath at 30°C for 10 min. Then, 2.4 mL of a freshly prepared 10 mM NaBH_4 solution was injected under vigorous stirring. A reddish solution was obtained after aging the samples over 5 days at 40°C . The seed solution can be stored for at least one month at room temperature. For the synthesis of AuBPs, 400 mL of 0.1 M CTAB solution was constituted, in which 4 mL of 10 mM AgNO_3 , 8 mL of 25 mM HAuCl_4 , and 8 mL of 1 M HCl were added in sequence under gentle stirring. Then 3200 μL of 100 mM AA solution was injected under vigorous stirring, followed by the addition of 3200 μL of seed solution when the solution turned colorless. The reaction mixture was left undisturbed at 30°C for 4 h. After synthesis, the particles were purified by at least 3 rounds of centrifugation and pellet redispersion in 2.5 mM CTAC.

Preparation of the PDMS Molds. The microtextured mold for the supercrystals was manufactured in PDMS (Sylgard 184, Dow Corning), following standard soft lithography techniques.^{38,77} The master was purchased from Blackhole lab and was composed of pillars having different shapes and sizes on a 4 in. silicon wafer covered with SU-8 resin. PDMS (10:1 elastomer to curing agent) was cured at 70°C for 3 h. In this work, assembly experiments were performed on (100) silicon wafers and glass coverslips.

Preparation of the Supercrystals. In all cases, a 10 μL drop of AuNR or AuBPs dispersion (400 mM in Au^0 and 2.5 mM CTAC) was deposited on the microtextured PDMS template and then

covered by the substrate. The solvent was subsequently allowed to evaporate to dryness (within 12 h), and the template was then removed, resulting in the formation of arrays of AuNR or AuBP supercrystals spread over millimeter-sized areas.

UV–Vis–NIR Absorbance Spectroscopy. The extinction of the gold nanoparticle samples was measured using a Cary 5000 UV–vis–NIR spectrometer at room temperature, using disposable polystyrene cuvettes with optical paths of 1 cm.

Electronic Microscopy. TEM images were obtained on 300 mesh carbon-coated copper grids using a JEOL 1400 microscope, operating at an acceleration voltage of 120 kV. SEM characterization was performed with a Zeiss Supra55VP instrument with an acceleration voltage of 5 keV.

SAXS Experiments. The supercrystal structures were probed by SAXS at the SWING beamline of the SOLEIL synchrotron (Saint-Aubin, France) using a beam energy of 16 keV and a sample-to-detector distance of 6.225 m. μSAXS was performed with a spot size of $20 \times 20 \mu\text{m}^2$, 12 keV and a sample-to-detector distance of 6.225 m. Some SAXS data were collected at the LPS using a rotating anode ($\text{Cu K}\alpha$, $\lambda = 1.542 \text{ \AA}$) and a sample-to-detector distance of 1.396 m. Data treatment (angular averaging and normalization) was done using the Nika 2D SAS macros in Igor Pro.⁷⁸

Simulations. We performed event-driven molecular dynamics simulations^{66,67} of hard spherocylinders confined by multiple flat hard walls forming either a triangular prism or a square prism. During the simulations, the system is slowly compressed from a dilute disordered phase by decreasing the position of the top confining wall with a constant velocity. As this compression heats the system, a thermostat was used to keep the temperature approximately constant. The simulation is stopped when the pressure in the system becomes so high that the numerical prediction of collisions between particles becomes inaccurate, at which point the system is essentially jammed. The speed of the top plate is set to $10^{-4} D/t$, with D being the rod diameter, $\tau = \sqrt{mD^2/k_B T}$ representing the time unit of the simulation, m is the particle mass, and $k_B T$ is the thermal energy. Faster compression speeds were also explored and for sufficiently large compression led to more disordered systems with a larger number of domains of aligned particles, as the system has less time to equilibrate during compression. Note that during compression, the edge length L_{box} of the ground plane of the prism remains constant. Due to the vertical compression, alignment of the particles can often be seen to change nonmonotonically with packing fraction as the particles self-assemble into a well-defined number of layers that are forced to tilt as the system is further compressed (see SI).

ASSOCIATED CONTENT

Supporting Information

The Supporting Information is available free of charge at <https://pubs.acs.org/doi/10.1021/acsnano.3c12799>.

TEM images of the gold nanorods and corresponding extinction spectra, SEM images of gold nanorods supercrystals, μSAXS characterization of the supercrystals, details on simulations, TEM images of the gold bipyramids and corresponding extinction spectra, and SEM images of gold bipyramids supercrystals (PDF)

AUTHOR INFORMATION

Corresponding Authors

Frank Smallenburg – *Université Paris-Saclay, CNRS, Laboratoire de Physique des Solides, 91405 Orsay, France;*

orcid.org/0000-0002-9401-6067;

Email: frank.smallenburg@cnrs.fr

Marianne Impéror-Clerc – *Université Paris-Saclay, CNRS, Laboratoire de Physique des Solides, 91405 Orsay, France;*

orcid.org/0000-0002-0269-7556;

Email: marianne.imperor@universite-paris-saclay.fr

Doru Constantin – Institut Charles Sadron, CNRS and Université de Strasbourg, 67034 Strasbourg, France; orcid.org/0000-0001-5623-9633; Email: constantin@unistra.fr

Cyrille Hamon – Université Paris-Saclay, CNRS, Laboratoire de Physique des Solides, 91405 Orsay, France; orcid.org/0000-0001-9529-9102; Email: cyrille.hamon@universite-paris-saclay.fr

Authors

Wajdi Chaâbani – Université Paris-Saclay, CNRS, Laboratoire de Physique des Solides, 91405 Orsay, France; orcid.org/0000-0003-1077-2752

Jieli Lyu – Université Paris-Saclay, CNRS, Laboratoire de Physique des Solides, 91405 Orsay, France; Present Address: School of Materials Science and Engineering, Xi'an University of Technology, Xi'an 710048, Shaanxi, People's Republic of China

Jules Marcone – Université Paris-Saclay, CNRS, Laboratoire de Physique des Solides, 91405 Orsay, France

Claire Goldmann – Université Paris-Saclay, CNRS, Laboratoire de Physique des Solides, 91405 Orsay, France

Eleonora J. M. ten Veen – Soft Condensed Matter, Debye Institute of Nanomaterials Science, Utrecht University, 3584 CC Utrecht, Netherlands

Clément Dumesnil – Université Paris-Saclay, CNRS, Laboratoire de Physique des Solides, 91405 Orsay, France; orcid.org/0009-0004-6907-0063

Thomas Bizien – SWING Beamline, SOLEIL Synchrotron, 91190 Gif-sur-Yvette, France; orcid.org/0000-0002-8779-7897

Complete contact information is available at:

<https://pubs.acs.org/10.1021/acsnano.3c12799>

Author Contributions

*These authors contributed equally (W.C. and J.L.).

Notes

The authors declare no competing financial interest.

ACKNOWLEDGMENTS

The CNRS is acknowledged for funding and support. The authors thanks Stéphan Rouzière for the use of the MORPHEUS platform. J.L. acknowledges financial support by the China Scholarship Council (CSC) for her Ph.D. J.M. acknowledges financial support by the ANR NIMROD Project (ANR-21-CE09-0019) for his Ph.D. C.H. and D.C. acknowledge financial support from the ANR METATRIP Project (ANR-22-CE09-0011). This work has benefited from an Investissements d'Avenir grant from Labex PALM (ANR-10-LABX-0039-PALM). The authors acknowledge SOLEIL for the provision of synchrotron radiation facilities (experiments 20201118, 20210006, and 20221057, SWING beamline) and particularly Javier Perez, Françoise Deschamps, and Youssef Liatimi for assistance during the experiments. The present work has benefited from the electronic microscopy facility of Imagerie-Gif (<http://www.i2bc.paris-saclay.fr>), member of IBiSA (<http://www.ibisa.net>), supported by "France-BioImaging" (ANR10-INBS-04-01) and the Labex "Saclay Plant Science" (ANR-11-IDEX-0003-02).

REFERENCES

- (1) Grason, G. M. Perspective: Geometrically Frustrated Assemblies. *J. Chem. Phys.* **2016**, *145*, No. 110901.
- (2) Sadoc, J.-F.; Mosseri, R. *Geometrical Frustration*. Cambridge University Press: Cambridge, 1999.
- (3) Dshemuchadse, J. Soft Matter Crystallography—Complex, Diverse, and New Crystal Structures in Condensed Materials on the Mesoscale. *J. Appl. Phys.* **2022**, *131*, No. 020901.
- (4) Hamon, C.; Liz-Marzán, L. M. Hierarchical Assembly of Plasmonic Nanoparticles. *Chem.—Eur. J.* **2015**, *21*, 9956–9963.
- (5) Vogel, N.; Retsch, M.; Fustin, C. A.; Del Campo, A.; Jonas, U. Advances in Colloidal Assembly: the Design of Structure and Hierarchy in Two and Three Dimensions. *Chem. Rev.* **2015**, *115*, 6265–311.
- (6) de Nijs, B.; Dussi, S.; Smalenburg, F.; Meeldijk, J. D.; Groenendijk, D. J.; Filion, L.; Imhof, A.; van Blaaderen, A.; Dijkstra, M. Entropy-Driven Formation of Large Icosahedral Colloidal Clusters by Spherical Confinement. *Nat. Mater.* **2015**, *14*, 56–60.
- (7) Galvan-Moya, J. E.; Altantzis, T.; Nelissen, K.; Peeters, F. M.; Grzelczak, M.; Liz-Marzán, L. M.; Bals, S.; Van Tendeloo, G. Self-Organization of Highly Symmetric Nanoassemblies: a Matter Of Competition. *ACS Nano* **2014**, *8*, 3869–75.
- (8) Kumacheva, E.; Golding, R. K.; Allard, M.; Sargent, E. H. Colloid Crystal Growth on Mesoscopically Patterned Surfaces: Effect of Confinement. *Adv. Mater.* **2002**, *14*, 221–224.
- (9) Damasceno, P. F.; Engel, M.; Glotzer, S. C. Predictive Self-Assembly of Polyhedra into Complex Structures. *Science* **2012**, *337*, 453–457.
- (10) Ming, T.; Kou, X.; Chen, H.; Wang, T.; Tam, H.-L.; Cheah, K.-W.; Chen, J.-Y.; Wang, J. Ordered Gold Nanostructure Assemblies Formed by Droplet Evaporation. *Angew. Chem. Inter. Ed.* **2008**, *120*, 9831–9836.
- (11) Torquato, S.; Jiao, Y. Dense Packings of the Platonic and Archimedean solids. *Nature* **2009**, *460*, 876–879.
- (12) Boles, M. A.; Engel, M.; Talapin, D. V. Self-Assembly of Colloidal Nanocrystals: from Intricate Structures to Functional Materials. *Chem. Rev.* **2016**, *116*, 11220–11289.
- (13) Lyu, J.; Chaabani, W.; Modin, E.; Chuvilin, A.; Bizien, T.; Smalenburg, F.; Imperor-Clerc, M.; Constantin, D.; Hamon, C. Double-Lattice Packing of Pentagonal Gold Bipyramids in Super-crystals with Triclinic Symmetry. *Adv. Mater.* **2022**, *34*, No. e2200883.
- (14) Wang, Y.; Chen, J.; Zhong, Y.; Jeong, S.; Li, R.; Ye, X. Structural Diversity in Dimension-Controlled Assemblies of Tetrahedral Gold Nanocrystals. *J. Am. Chem. Soc.* **2022**, *144*, 13538–13546.
- (15) Sacanna, S.; Pine, D. J.; Yi, G.-R. Engineering Shape: the Novel Geometries of Colloidal Self-Assembly. *Soft Matter* **2013**, *9*, 8096–8106.
- (16) Wang, D.; Hermes, M.; Kotni, R.; Wu, Y.; Tasios, N.; Liu, Y.; de Nijs, B.; van der Wee, E. B.; Murray, C. B.; Dijkstra, M.; van Blaaderen, A. Interplay Between Spherical Confinement and Particle Shape on the Self-Assembly of Rounded Cubes. *Nat. Commun.* **2018**, *9*, 2228.
- (17) Monderkamp, P. A.; Wittmann, R.; Cortes, L. B. G.; Aarts, D. G. A. L.; Smalenburg, F.; Löwen, H. Topology of Orientational Defects in Confined Smectic Liquid Crystals. *Phys. Rev. Lett.* **2021**, *127*, No. 198001.
- (18) Schyck, S.; Meijer, J.-M.; Baldauf, L.; Schall, P.; Petukhov, A. V.; Rossi, L. Self-Assembly of Colloidal Superballs under Spherical Confinement of a Drying Droplet. *JCI Open* **2022**, *5*, No. 100037.
- (19) Parker, R. M.; Frka-Petesic, B.; Guidetti, G.; Kamita, G.; Consani, G.; Abell, C.; Vignolini, S. Hierarchical Self-Assembly of Cellulose Nanocrystals in a Confined Geometry. *ACS Nano* **2016**, *10*, 8443–8449.
- (20) Li, Y.; Jun-Yan Suen, J.; Prince, E.; Larin, E. M.; Klinkova, A.; Thérien-Aubin, H.; Zhu, S.; Yang, B.; Helmy, A. S.; Lavrentovich, O. D.; Kumacheva, E. Colloidal Cholesteric Liquid Crystal in Spherical Confinement. *Nat. Commun.* **2016**, *7*, 12520.
- (21) Grzelczak, M.; Sanchez-Iglesias, A.; Mezerji, H. H.; Bals, S.; Perez-Juste, J.; Liz-Marzán, L. M. Steric Hindrance Induces Crosslike Self-Assembly of Gold Nanodumbbells. *Nano Lett.* **2012**, *12*, 4380–4.
- (22) Manoharan, V. N. Colloidal Matter: Packing, Geometry, and Entropy. *Science* **2015**, *349*, 6251.

- (23) Teich, E. G.; van Anders, G.; Klotsa, D.; Dshemuchadse, J.; Glotzer, S. C. Clusters of polyhedra in spherical confinement. *Proc. Natl. Acad. Sci. U.S.A.* **2016**, *113*, E669–E678.
- (24) Wang, D.; Hermes, M.; Najm, S.; Tasios, N.; Grau-Carbonell, A.; Liu, Y.; Bals, S.; Dijkstra, M.; Murray, C. B.; van Blaaderen, A. Structural Diversity in Three-Dimensional Self-Assembly of Nanoplatelets by Spherical Confinement. *Nat. Commun.* **2022**, *13*, 6001.
- (25) Jedrych, A.; Pawlak, M.; Gorecka, E.; Lewandowski, W.; Wojcik, M. M. Light-Responsive Supramolecular Nanotubes-Based Chiral Plasmonic Assemblies. *ACS Nano* **2023**, *17*, 5548–5560.
- (26) Wan, S.; Xi, X.; Zhang, H.; Ning, J.; Zheng, Z.; Zhang, Z.; Long, Y.; Deng, Y.; Fan, P.; Yang, D.; Li, T.; Dong, A. Shape-Mediated Oriented Assembly of Concave Nanoparticles under Cylindrical Confinement. *ACS Nano* **2022**, *16*, 21315–21323.
- (27) Bai, P.; Yang, S.; Bao, W.; Kao, J.; Thorkelsson, K.; Salmeron, M. B.; Zhang, X.; Xu, T. Diversifying Nanoparticle Assemblies in Supramolecule Nanocomposites Via Cylindrical Confinement. *Nano Lett.* **2017**, *17*, 6847–6854.
- (28) Cortes, L. B. G.; Gao, Y.; Dullens, R. P. A.; Aarts, D. G. A. L. Colloidal Liquid Crystals in Square Confinement: Isotropic, Nematic and Smectic Phases. *J. Phys.: Condens. Matter* **2017**, *29*, No. 064003.
- (29) Lewis, A. H.; Garlea, I.; Alvarado, J.; Dammone, O. J.; Howell, P. D.; Majumdar, A.; Mulder, B. M.; Lettinga, M. P.; Koenderink, G. H.; Aarts, D. G. A. L. Colloidal Liquid Crystals in Rectangular Confinement: Theory and Experiment. *Soft Matter* **2014**, *10*, 7865–7873.
- (30) Giannini, V.; Fernández-Domínguez, A. I.; Heck, S. C.; Maier, S. A. Plasmonic Nanoantennas: Fundamentals and Their Use in Controlling the Radiative Properties of Nanoemitters. *Chem. Rev.* **2011**, *111*, 3888–3912.
- (31) Alvarez-Puebla, R.; Liz-Marzán, L. M.; García de Abajo, F. J. Light Concentration at the Nanometer Scale. *J. Phys. Chem. Lett.* **2010**, *1*, 2428–2434.
- (32) García-Lojo, D.; Nunez-Sanchez, S.; Gomez-Grana, S.; Grzelczak, M.; Pastoriza-Santos, I.; Perez-Juste, J.; Liz-Marzan, L. M. Plasmonic Supercrystals. *Acc. Chem. Res.* **2019**, *52*, 1855–1864.
- (33) Ghosh, S. K.; Pal, T. Interparticle Coupling Effect on the Surface Plasmon Resonance of Gold Nanoparticles: From Theory to Applications. *Chem. Rev.* **2007**, *107*, 4797–4862.
- (34) Pileni, M.-P. Self-Assemblies of Gold Nanocrystals: Unexpected Properties. *J. Phys. Chem. C* **2021**, *125*, 25936–25950.
- (35) Gates, B. D.; Xu, Q.; Stewart, M.; Ryan, D.; Willson, C. G.; Whitesides, G. M. New Approaches to Nanofabrication: Molding, Printing, and Other Techniques. *Chem. Rev.* **2005**, *105*, 1171–1196.
- (36) Kim, E.; Xia, Y.; Whitesides, G. M. Polymer Microstructures Formed by Moulding in Capillaries. *Nature* **1995**, *376*, 581–584.
- (37) Xia, Y.; Whitesides, G. M. Soft Lithography. *Angew. Chem. Int. Ed.* **1998**, *37*, 550–575.
- (38) Qin, D.; Xia, Y. N.; Whitesides, G. M. Soft lithography for Micro- and Nanoscale Patterning. *Nat. Protoc.* **2010**, *5*, 491–502.
- (39) Vila-Liarte, D.; Feil, M. W.; Manzi, A.; Garcia-Pomar, J. L.; Huang, H.; Dobliger, M.; Liz-Marzan, L. M.; Feldmann, J.; Polavarapu, L.; Mihi, A. Templated-Assembly of CsPbBr₃ Perovskite Nanocrystals into 2D Photonic Supercrystals with Amplified Spontaneous Emission. *Angew. Chem., Int. Ed.* **2020**, *59*, 17750–17756.
- (40) Pazos-Perez, N.; Ni, W.; Schweikart, A.; Alvarez-Puebla, R. A.; Fery, A.; Liz-Marzan, L. M. Highly Uniform SERS Substrates Formed by Wrinkle-Confined Drying of Gold Colloids. *Chem. Sci.* **2010**, *1*, 174–178.
- (41) Kraus, T.; Brodoceanu, D.; Pazos-Perez, N.; Fery, A. Colloidal Surface Assemblies: Nanotechnology Meets Bioinspiration. *Adv. Funct. Mater.* **2013**, *23*, 4529–4541.
- (42) Hamon, C.; Postic, M.; Mazari, E.; Bizien, T.; Dupuis, C.; Even-Hernandez, P.; Jimenez, A.; Courbin, L.; Gosse, C.; Artzner, F.; Marchi-Artzner, V. Three-Dimensional Self-Assembling of Gold Nanorods with Controlled Macroscopic Shape and Local Smectic B Order. *ACS Nano* **2012**, *6*, 4137–4146.
- (43) Han, W.; Lin, Z. Learning from “Coffee Rings”: Ordered Structures Enabled by Controlled Evaporative Self-Assembly. *Angew. Chem. Int. Ed.* **2012**, *51*, 1534–1546.
- (44) Li, F.; Josephson, D. P.; Stein, A. Colloidal Assembly: The Road from Particles to Colloidal Molecules and Crystals. *Angew. Chem. Int. Ed.* **2011**, *50*, 360–388.
- (45) Holzner, F.; Kuemin, C.; Paul, P.; Hedrick, J. L.; Wolf, H.; Spencer, N. D.; Duerig, U.; Knoll, A. W. Directed Placement of Gold Nanorods Using a Removable Template for Guided Assembly. *Nano Lett.* **2011**, *11*, 3957–3962.
- (46) Yan, B.; Thubagere, A.; Premasiri, W. R.; Ziegler, L. D.; Dal Negro, L.; Reinhard, B. M. Engineered SERS Substrates with Multiscale Signal Enhancement: Nanoparticle Cluster Arrays. *ACS Nano* **2009**, *3*, 1190–1202.
- (47) Zhang, H.; Liu, Y.; Shahidan, M. F. S.; Kinnear, C.; Maasoumi, F.; Cadusch, J.; Akinoglu, E. M.; James, T. D.; Widmer-Cooper, A.; Roberts, A.; Mulvaney, P. Direct Assembly of Vertically Oriented, Gold Nanorod Arrays. *Adv. Funct. Mater.* **2021**, *31*, 2006753.
- (48) Matricardi, C.; Hanske, C.; Garcia-Pomar, J. L.; Langer, J.; Mihi, A.; Liz-Marzán, L. M. Gold Nanoparticle Plasmonic Superlattices as Surface-Enhanced Raman Spectroscopy Substrates. *ACS Nano* **2018**, *12*, 8531–8539.
- (49) Scarabelli, L.; Vila-Liarte, D.; Mihi, A.; Liz-Marzán, L. M. Templated Colloidal Self-Assembly for Lattice Plasmon Engineering. *Acc. Mater. Res.* **2021**, *2*, 816–827.
- (50) Gupta, V.; Probst, P. T.; Gößler, F. R.; Steiner, A. M.; Schubert, J.; Brasse, Y.; König, T. A. F.; Fery, A. Mechanotunable Surface Lattice Resonances in the Visible Optical Range by Soft Lithography Templates and Directed Self-Assembly. *ACS Appl. Mater.* **2019**, *11*, 28189–28196.
- (51) Hanske, C.; Hill, E. H.; Vila-Liarte, D.; González-Rubio, G.; Matricardi, C.; Mihi, A.; Liz-Marzán, L. M. Solvent-Assisted Self-Assembly of Gold Nanorods into Hierarchically Organized Plasmonic Mesostuctures. *ACS Appl. Mater.* **2019**, *11*, 11763–11771.
- (52) Charconnet, M.; Kuttner, C.; Plou, J.; García-Pomar, J. L.; Mihi, A.; Liz-Marzán, L. M.; Seifert, A. Mechanically Tunable Lattice-Plasmon Resonances by Templated Self-Assembled Superlattices for Multi-Wavelength Surface-Enhanced Raman Spectroscopy. *Small Methods* **2021**, *5*, 2100453.
- (53) Kravets, V. G.; Kabashin, A. V.; Barnes, W. L.; Grigorenko, A. N. Plasmonic Surface Lattice Resonances: A Review of Properties and Applications. *Chem. Rev.* **2018**, *118*, 5912–5951.
- (54) Thai, T.; Zheng, Y.; Ng, S. H.; Mudie, S.; Altissimo, M.; Bach, U. Self-Assembly of Vertically Aligned Gold Nanorod Arrays on Patterned Substrates. *Angew. Chem., Int. Ed.* **2012**, *51*, 8732–8735.
- (55) Alba, M.; Pazos-Perez, N.; Vaz, B.; Formentin, P.; Tebbe, M.; Correa-Duarte, M. A.; Granero, P.; Ferré-Borrull, J.; Alvarez, R.; Pallares, J.; Fery, A.; de Lera, A. R.; Marsal, L. F.; Alvarez-Puebla, R. A. Macroscale Plasmonic Substrates for Highly Sensitive Surface-Enhanced Raman Scattering. *Angew. Chem., Int. Ed.* **2013**, *52*, 6459–6463.
- (56) Cho, W. J.; Kim, Y.; Kim, J. K. Ultrahigh-Density Array of Silver Nanoclusters for SERS Substrate With High Sensitivity and Excellent Reproducibility. *ACS Nano* **2012**, *6*, 249–55.
- (57) Bodelon, G.; Montes-García, V.; Lopez-Puente, V.; Hill, E. H.; Hamon, C.; Sanz-Ortiz, M. N.; Rodal-Cedeira, S.; Costas, C.; Celiksoy, S.; Perez-Juste, I.; Scarabelli, L.; La Porta, A.; Perez-Juste, J.; Pastoriza-Santos, I.; Liz-Marzan, L. M. Detection and Imaging of Quorum Sensing in *Pseudomonas Aeruginosa* Biofilm Communities by Surface-Enhanced Resonance Raman Scattering. *Nat. Mater.* **2016**, *15*, 1203–1211.
- (58) Wei, W.; Bai, F.; Fan, H. Oriented Gold Nanorod Arrays: Self-Assembly and Optoelectronic Applications. *Angew. Chem., Int. Ed.* **2019**, *58*, 11956–11966.
- (59) Langer, J.; Jimenez de Aberasturi, D.; Aizpurua, J.; Alvarez-Puebla, R. A.; Auguie, B.; Baumberg, J. J.; Bazan, G. C.; Bell, S. E. J.; Boisen, A.; Brolo, A. G.; Choo, J.; Cialla-May, D.; Deckert, V.; Fabris, L.; Faulds, K.; García de Abajo, F. J.; Goodacre, R.; Graham, D.; Haes,

- A. J.; Haynes, et al. Present and Future of Surface-Enhanced Raman Scattering. *ACS Nano* **2020**, *14*, 28–117.
- (60) Jägeler-Hoheisel, T.; Cordeiro, J.; Lecarme, O.; Cuche, A.; Girard, C.; Dujardin, E.; Peyrade, D.; Arbouet, A. Plasmonic Shaping in Gold Nanoparticle Three-Dimensional Assemblies. *J. Phys. Chem. C* **2013**, *117*, 23126–23132.
- (61) Hamon, C.; Novikov, S.; Scarabelli, L.; Basabe-Desmonts, L.; Liz-Marzán, L. M. Hierarchical Self-Assembly of Gold Nanoparticles into Patterned Plasmonic Nanostructures. *ACS Nano* **2014**, *8*, 10694–10703.
- (62) Hamon, C.; Sanz-Ortiz, M. N.; Modin, E.; Hill, E. H.; Scarabelli, L.; Chuvilin, A.; Liz-Marzán, L. M. Hierarchical Organization and Molecular Diffusion in Gold Nanorod/Silica Supercrystal Nanocomposites. *Nanoscale* **2016**, *8*, 7914–7922.
- (63) Schulz, F.; Lokteva, I.; Parak, W. J.; Lehmkuhler, F. Recent Notable Approaches to Study Self-Assembly of Nanoparticles with X-Ray Scattering and Electron Microscopy. *Part. Part. Syst. Charact.* **2021**, *38*, 2100087.
- (64) García-Lojo, D.; Modin, E.; Gómez-Graña, S.; Impérator-Clerc, M.; Chuvilin, A.; Pastoriza-Santos, I.; Pérez-Juste, J.; Constantin, D.; Hamon, C. Structure and Formation Kinetics of Millimeter-Size Single Domain Supercrystals. *Adv. Funct. Mater.* **2021**, *31*, 2101869.
- (65) Xiao, J.; Li, Z.; Ye, X.; Ma, Y.; Qi, L. Self-Assembly of Gold Nanorods into Vertically Aligned, Rectangular Microplates with a Supercrystalline Structure. *Nanoscale* **2014**, *6*, 996–1004.
- (66) Smalenburg, F.; Löwen, H. Close Packing of Rods on Spherical Surfaces. *J. Chem. Phys.* **2016**, *144*, na.
- (67) Hernández de la Peña, L.; van Zon, R.; Schofield, J.; Opps, S. B. Discontinuous Molecular Dynamics for Semiflexible and Rigid Bodies. *J. Chem. Phys.* **2007**, *126*, na.
- (68) Marccone, J.; Chaabani, W.; Goldmann, C.; Imperor-Clerc, M.; Constantin, D.; Hamon, C. Polymorphous Packing of Pentagonal Nanoprisms. *Nano Lett.* **2023**, *23*, 1337–1342.
- (69) Kim, F.; Connor, S.; Song, H.; Kuykendall, T.; Yang, P. Platonic Gold Nanocrystals. *Angew. Chem. Inter. Ed.* **2004**, *43*, 3673–3677.
- (70) Scarabelli, L.; Sun, M.; Zhuo, X.; Yoo, S.; Millstone, J. E.; Jones, M. R.; Liz-Marzán, L. M. Plate-Like Colloidal Metal Nanoparticles. *Chem. Rev.* **2023**, *123*, 3493–3542.
- (71) Dey, A.; Ye, J.; De, A.; Debroye, E.; Ha, S. K.; Bladt, E.; Kshirsagar, A. S.; Wang, Z.; Yin, J.; Wang, Y.; Quan, L. N.; Yan, F.; Gao, M.; Li, X.; Shamsi, J.; Debnath, T.; Cao, M.; Scheel, M. A.; Kumar, S.; et al. State of the Art and Prospects for Halide Perovskite Nanocrystals. *ACS Nano* **2021**, *15*, 10775–10981.
- (72) Abecassis, B.; Tessier, M. D.; Davidson, P.; Dubertret, B. Self-Assembly of CdSe Nanoplatelets into Giant Micrometer-Scale Needles Emitting Polarized Light. *Nano Lett.* **2014**, *14*, 710–5.
- (73) Kovalenko, M. V.; Manna, L.; Cabot, A.; Hens, Z.; Talapin, D. V.; Kagan, C. R.; Klimov, V. I.; Rogach, A. L.; Reiss, P.; Milliron, D. J.; Guyot-Sionnest, P.; Konstantatos, G.; Parak, W. J.; Hyeon, T.; Korgel, B. A.; Murray, C. B.; Heiss, W. Prospects of Nanoscience with Nanocrystals. *ACS Nano* **2015**, *9*, 1012–57.
- (74) Zanella, M.; Gomes, R.; Povia, M.; Giannini, C.; Zhang, Y.; Riskin, A.; Van Bael, M.; Hens, Z.; Manna, L. Self-Assembled Multilayers of Vertically Aligned Semiconductor Nanorods on Device-Scale Areas. *Adv. Mater.* **2011**, *23*, 2205–2209.
- (75) Scarabelli, L.; Grzelczak, M.; Liz-Marzán, L. M. Tuning Gold Nanorod Synthesis through Prereduction with Salicylic Acid. *Chem. Mater.* **2013**, *25*, 4232–4238.
- (76) Sanchez-Iglesias, A.; Winckelmans, N.; Altantzis, T.; Bals, S.; Grzelczak, M.; Liz-Marzán, L. M. High-Yield Seeded Growth of Monodisperse Pentatwinned Gold Nanoparticles through Thermally Induced Seed Twinning. *J. Am. Chem. Soc.* **2017**, *139*, 107–110.
- (77) McDonald, J. C.; Duffy, D. C.; Anderson, J. R.; Chiu, D. T.; Wu, H.; Schueller, O. J.; Whitesides, G. M. Fabrication of Microfluidic Systems in Poly(dimethylsiloxane). *Electrophoresis* **2000**, *21*, 27–40.
- (78) Ilavsky, J. Nika: Software for Two-Dimensional Data Reduction. *J. Appl. Crystallogr.* **2012**, *45*, 324–328.